Available online at www.sciencedirect.com
SCIENCE DIRECT®

ELSEVIER

Bulletin of Mathematical Biology 67 (2005) 137–168

Bulletin of Mathematical Biology

www.elsevier.com/locate/ybulm

A study of bacterial flagellar bundling

Heather Flores[a], Edgar Lobaton[b], Stefan Méndez-Diez[c],
Svetlana Tlupova[d], Ricardo Cortez[d,*]

[a] *Department of Mathematics, University of Nebraska, 203 Avery Hall, P.O. Box 880130, Lincoln, NE 68588, USA*
[b] *Department of Mathematics, University of California at Berkeley, 970 Evans Hall #3840, Berkeley, CA 94720, USA*
[c] *Department of Applied Mathematics and Scientific Computing, University of Maryland, 3103 Mathematics Building, College Park, MD 20742, USA*
[d] *Department of Mathematics, Tulane University, 6823 St. Charles Avenue, #424, New Orleans, LA 70118, USA*

Received 3 November 2003; accepted 30 June 2004

Abstract

Certain bacteria, such as *Escherichia coli* (*E. coli*) and *Salmonella typhimurium* (*S. typhimurium*), use multiple flagella often concentrated at one end of their bodies to induce locomotion. Each flagellum is formed in a left-handed helix and has a motor at the base that rotates the flagellum in a corkscrew motion. We present a computational model of the flagellar motion and their hydrodynamic interaction. The model is based on the equations of Stokes flow to describe the fluid motion. The elasticity of the flagella is modeled with a network of elastic springs while the motor is represented by a torque at the base of each flagellum. The fluid velocity due to the forces is described by regularized Stokeslets and the velocity due to the torques by the associated regularized rotlets. Their expressions are derived. The model is used to analyze the swimming motion of a single flagellum and of a group of three flagella in close proximity to one another. When all flagellar motors rotate counterclockwise, the hydrodynamic interaction can lead to bundling. We present an analysis of the flow surrounding the flagella. When at least one of the motors changes its direction of rotation, the same initial conditions lead to a tumbling behavior characterized by the separation of the flagella,

---

* Corresponding author.
E-mail addresses: hflores@math.unl.edu (H. Flores), edgar_loba@yahoo.com (E. Lobaton), stefan@alumni.uchicago.edu (S. Méndez-Diez), tlupova@tulane.edu (S. Tlupova), cortez@math.tulane.edu (R. Cortez).

doi:10.1016/j.bulm.2004.06.006

changes in their orientation, and no net swimming motion. The analysis of the flow provides some intuition for these processes.

1. Introduction

Single-celled bacteria, such as *Escherichia coli* (*E. coli*) induce locomotion through the use of multiple flagella often concentrated at one end of the organism. Each flagellum is flexible and maintains roughly a left-handed helical shape. At the base of each flagellum is a small rotary motor that can turn clockwise or counterclockwise. It is known that when the motors all turn counterclockwise (when viewed from behind the flagella), the flagella tend to gather together to form a single helix [see for example Turner et al. (2000)]. This movement, known as bundling, results in forward motion of the cell. When some or all of the motors turn clockwise, the flagella go through a sequence of shape transformations changing amplitude, pitch, and sometimes handedness. The consequence is that the bundle unravels and the flagella separate. This motion is known as tumbling and changes the movement of the organism into one without a preferred direction, resulting in no appreciable net motion (Berg, 2003). Bundling and tumbling together enable the organism to move in one direction and reorient itself to move in another direction where there may be more favorable conditions for survival. This process may be in response to chemical stimuli (chemotaxis) or other factors such as temperature and light intensity.

Previous work on the modeling of helical swimming motions has combined analytical and numerical methods and has focused mainly on organisms with a single flagellum. Lighthill (1976, 1996) provided mathematical analysis of the motion of a thin tube with helical shape using slender-body theory. In this theory, the flagellum is replaced with a distribution of Stokeslets and dipoles along its centerline. The analysis provided refined resistance coefficients for this motion and modifications to account approximately for the drag force on the cell body. Higdon (1979a,b) combined mathematical and numerical analyses applied to the motion of an organism with a spherical body and a single flagellum. The flagellum was also modeled using slender-body approximations. The body was assumed to be spherical which allowed the use of images to impose approximate boundary conditions on its surface. A rotlet at the center of the cell body was included in order to balance the rotation induced by the flagellum. Ramia et al. (1993) used a computational approach based on the boundary element method to model the motion of an organism with spherical body and a single helical flagellum. Their study included motions near walls and near another organism of the same shape. The description of the organism is similar to that in Higdon (1979b); however, the Green's function approach is traded for a boundary element method in order to address cases with multiple walls (of finite extent) and multiple organisms. Goto et al. (2001) also use the boundary element method to compute the swimming speed and cell body rotation of a singly-flagellated bacterium. Given the angular velocity of the motor, the geometry of the cell body and flagellum, and assuming both move as rigid bodies, they are able to compute the six unknowns that represent the swimming velocity and angular velocity of the cell body. These computations are not dynamic. Goto et al. (1999) performed computations using a cell body and three flagella using the same boundary element method as in Goto et al. (2001); however, the dynamics of the motion, particularly bundling, were not addressed since only the linear and angular velocities of the cell body were determined from a static balance of forces and torques.

The works mentioned above assumed from the outset the shape of the flagellum for all time. For helical waves, the centerline was assumed to be given by a helix of the form

$$(x, y, z) = (x, E(x)\cos(kx - \omega t), E(x)\sin(kx - \omega t))$$

which implies that throughout the motion, the flagellum rotates and translates as a solid body without deformation. This assumption simplifies the mathematical analysis but is not realistic for bacteria like *E. coli* and *S. typhimurium*, whose flagella should not be considered rigid screws since they assume a variety of distinct helices depending on their environment [see for example Kamiya and Asakura (1976)].

Powers (2002) considered a single straight but flexible filament which is rotated at one end in a circular fashion around an axis parallel but not coincident with the filament. The rotation simulates the cell body rotation and the filament represents a single flagellum. Based on steady states of the filament driven by various rotation frequencies, conclusions were drawn regarding the possibility of bundling. However, only a single filament was considered and the hydrodynamic interactions among neighboring flagella were not taken into account. The Stokes flow was included only through the use of a transverse friction coefficient following local resistive-force theory (for a rod) and slender-body approximations, and the conclusions were based on the helical shape of the rotating isolated filament.

While some of the works cited above apply only to eukaryotic flagella and some may apply also to prokaryotic ones, the goal of the present study is to determine conditions that tend to produce bundling of various prokaryotic flagella in close proximity to one another. The emphasis here is on the role of the hydrodynamic interaction of the flagella in the processes of bundling and tumbling. No restrictions on the wave amplitudes or flagellum dimensions are imposed. In this way, the methodology used here can also be applied to other organisms that may not be slender or that display large-amplitude waves in their motion. It is important not to assume a priori the helical shape of the flagella for all time but allow for deformations during the interactions. Therefore, our model includes a mechanism designed to provide a certain amount of elasticity to the flagellum so that a helical shape is preferred but deviations from it are allowed. The simulations are based on solutions of Stokes equations in the presence of external forces given by shape functions that smoothly approximate delta distributions. This is the basis of the method of regularized Stokeslet (Cortez, 2001; Cortez et al., in press) used here. In addition, the rotation induced by the motors at the base of each flagellum is modeled with a *regularized rotlet* which is derived as the antisymmetric part of the derivative of the regularized Stokeslet. The rotlet represents a localized torque.

Table 1
Factors for the conversion from dimensionless units to dimensional variables

Dimensionless variable	Multiply by
Length	$\mathcal{L} = 10^{-5}$ m
Velocity	$U = 10^{-1}$ m s^{-1}
Time	$T = 10^{-4}$ s
Angular velocity	$T^{-1} = 10^{4}$ s^{-1}
Force density	$F = \mu U/\mathcal{L}^2 = 10^6$ N m^{-3}
Torque density	$T_q = \mu U/\mathcal{L} = 10$ N m^{-2}

We note that the force (torque) density is the force (torque) per unit volume.

2. Equations

The fluid dynamics in problems of microorganism motion, where length and velocity scales are very small, is well-modeled by the Stokes equations for incompressible flows

$$0 = -\nabla\tilde{P} + \mu\Delta\tilde{\mathbf{u}} + \tilde{\mathbf{f}}$$
$$0 = \nabla \cdot \tilde{\mathbf{u}}$$

where $\tilde{P}$ is the fluid pressure, $\tilde{\mathbf{u}}$ is the fluid velocity, μ is the viscosity of the fluid and $\tilde{\mathbf{f}}$ is the external force density. If we define $\mathcal{L}$ and U to be a characteristic length and a characteristic speed in the problem, we can define the dimensionless variables

$$\mathbf{x} = \frac{1}{\mathcal{L}}\tilde{\mathbf{x}}, \qquad \mathbf{u} = \frac{1}{U}\tilde{\mathbf{u}}, \qquad P = \frac{\mathcal{L}}{\mu U}\tilde{P}, \qquad \mathbf{f} = \frac{\mathcal{L}^2}{\mu U}\tilde{\mathbf{f}}.$$

Then, after some simplification, the Stokes equations in dimensionless form become

$$0 = -\nabla P + \Delta\mathbf{u} + \mathbf{f} \tag{1}$$
$$0 = \nabla \cdot \mathbf{u}. \tag{2}$$

These are the equations we use in our model. We mention that a typical length of an *E. coli* flagellum is 10–20 μm (Turner et al., 2000; Kim et al., 2003). A typical forward swimming speed of the cells is 10–40 μm s^{-1} (Turner et al., 2000; McClaine and Ford, 2002) and the motor rotation is on the order of 100 Hz (revolutions per second) (Turner et al., 2000; Berry, 2001; Berg, 2003; Kim et al., 2003). All computations will be performed using dimensionless variables. In all cases, the dimensional values will be computed using the viscosity of water, $\mu = 10^{-3}$ kg m^{-1} s^{-1} and the following parameters: $\mathcal{L} = 10^{-5}$ m and $U = 10^{-1}$ m s^{-1}. The last two values provide a time scale of $T = \mathcal{L}/U = 10^{-4}$ s. Table 1 shows explicitly the conversion factors used throughout this article.

2.1. Solutions of the Stokes equations

When a force $\mathbf{f}$ is exerted on the fluid, the resulting velocity field $\mathbf{u}$ and pressure P are the solution of Eqs. (1) and (2). The particular case of a single point force $\mathbf{f}_0$ exerted at $\mathbf{x}_0$ results in a velocity field called a *Stokeslet* and is given by

$$\mathbf{U}_s(\mathbf{x};\mathbf{x}_0,\mathbf{f}_0) = \frac{\mathbf{f}_0}{8\pi r} + \frac{[\mathbf{f}_0\cdot(\mathbf{x}-\mathbf{x}_0)](\mathbf{x}-\mathbf{x}_0)}{8\pi r^3}$$

where $r = \|\mathbf{x} - \mathbf{x}_0\|$. Note that this flow is undefined at $\mathbf{x} = \mathbf{x}_0$ although a distribution of forces on a surface yields a flow that is defined everywhere.

Our computations show the motion of a flagellum or a group of flagella without a body (or head). The motion is generated by forces along the surfaces of the flagella and by a torque at the base of each. The torque represents the one transferred to the flagellum by the motor at the junction with the body of the bacterium, which is currently not part of the model. The forces, based on points and springs, are designed to keep the flagellum in approximately the same helical shape while providing some flexibility to it. These are described in the next section.

The velocity field that satisfies Stokes equations when a torque $\mathbf{L}_0$ is applied at a single point $\mathbf{x}_0$ is called a *rotlet* and is given by

$$\mathbf{U}_r(\mathbf{x}; \mathbf{x}_0, \mathbf{L}_0) = \frac{\mathbf{L}_0 \times (\mathbf{x} - \mathbf{x}_0)}{8\pi r^3}. \tag{3}$$

This flow is more singular than the Stokeslet and is no longer integrable even if it were distributed over a surface. This implies that the fluid velocity becomes arbitrarily large as the evaluation point approaches the point where the torque is applied. In our computations, the rotlets will be placed at specific points in the fluid domain, and therefore, we will have to compute the fluid velocity at points arbitrarily close to the rotlet location.

The singularities in the velocity expression are due to the assumption of having point-forces and point-torques. However, the singularities can be eliminated through the systematic regularization of the flows described above by considering forces and torques that are applied not at single points but within small spheres centered at those points. In this way, the forces and torques are highly concentrated but are spread over a small neighborhood of the application points. The precise form of the force is given by a cutoff function $\phi_\delta(\mathbf{x})$ which we will take to be radially symmetric and to satisfy

$$\iiint_{\mathbb{R}^3} \phi_\delta(\mathbf{x})\, \mathrm{d}\mathbf{x} = 1,$$

where δ is a numerical parameter that controls the spread of the function (see Fig. 1). Throughout this article, we will use the cutoff function

$$\phi_\delta(\mathbf{x}) = \frac{15\delta^4}{8\pi(r^2 + \delta^2)^{7/2}} \tag{4}$$

where $r = \|\mathbf{x}\|$.

When the force in Eq. (1) is given by a cutoff centered at $\mathbf{x}_0$, $\mathbf{f}(\mathbf{x}) = \mathbf{f}_0\phi_\delta(\mathbf{x} - \mathbf{x}_0)$, one can derive the exact solution of the Stokes equation to get the *regularized Stokeslet* (see Appendix A).

$$\mathbf{U}_{\delta,s}(\mathbf{x}; \mathbf{x}_0, \mathbf{f}_0) = \frac{\mathbf{f}_0(r^2 + 2\delta^2)}{8\pi(r^2 + \delta^2)^{3/2}} + \frac{[\mathbf{f}_0 \cdot (\mathbf{x} - \mathbf{x}_0)](\mathbf{x} - \mathbf{x}_0)}{8\pi(r^2 + \delta^2)^{3/2}}. \tag{5}$$

Notice that as δ approaches zero, we recover the Stokeslet expression. However, the regularized Stokeslet represents a flow that is bounded for all $\mathbf{x}$ as long as $\delta > 0$. Regardless of the value of δ, the regularized Stokeslet in Eq. (5) is an exact solution of the Stokes equation for the given form of the force.

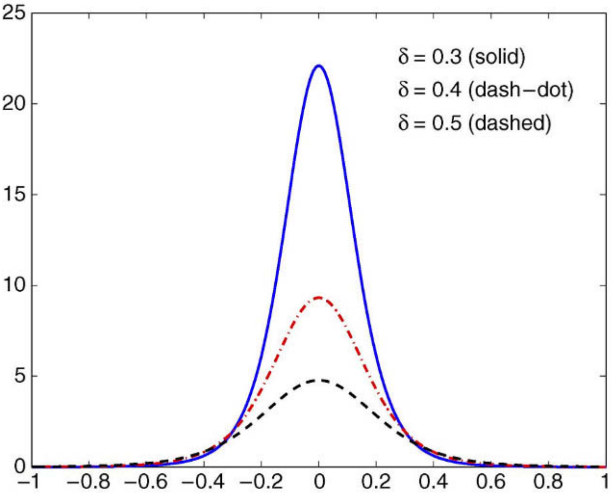

Fig. 1. The cutoff function in Eq. (4) for three values of δ.

The associated regularized rotlet is derived from the antisymmetric part of a directional derivative of the regularized Stokeslet (see Appendix A). The result for a torque $\mathbf{L}_0$ centered at $\mathbf{x}_0$ is

$$\mathbf{U}_{\delta,r}(\mathbf{x};\mathbf{x}_0,\mathbf{L}_0) = \frac{(2r^2+5\delta^2)}{16\pi(r^2+\delta^2)^{5/2}}[\mathbf{L}_0 \times (\mathbf{x}-\mathbf{x}_0)]. \tag{6}$$

Here too, as $\delta \to 0$ we recover the original rotlet expression. It is important to emphasize that the regularized rotlet yields finite velocities everywhere simply because of the assumed form of the torque. At points far from the torque, the regularized expression is nearly indistinguishable from the singular counterpart. Near the torque, the regularized expression provides a model for the fluid motion that can be used in computations.

3. The numerical method

In order to build the model, we start by creating the structure of the flagellum. Each flagellum is a tubular structure made of discrete particles connected by springs. Some of the springs connect particles around the cross-sections and others connect particles between neighboring cross-sections. The forces between two connected particles, $\mathbf{x}_j$ and $\mathbf{x}_k$, are computed using Hooke's Law:

$$\mathbf{f}_{jk} = \frac{k_0}{L_0^{jk}}(L^{jk}-L_0^{jk})\frac{\mathbf{x}_k-\mathbf{x}_j}{L^{jk}}, \qquad \mathbf{f}_{kj} = -\mathbf{f}_{jk}, \qquad L^{jk} = \|\mathbf{x}_k-\mathbf{x}_j\| \tag{7}$$

where k_0 is the stiffness constant, L^{jk} is defined to be the distance between $\mathbf{x}_k$ and $\mathbf{x}_j$ at time t, and the spring resting length, L_0^{jk}, is defined to be the initial distance between $\mathbf{x}_k$ and $\mathbf{x}_j$, so at time $t = 0$ the force between the particles is zero. Since the torque models the effect of the motor, it is applied only at one point at the base of each flagellum. When the torque is applied and the particles that describe the flagellum move, the distance between them changes, activating spring forces applied to both particles at the spring endpoints, in equal and opposite pairs. In this way, the total force is always zero. The forces are designed to maintain approximately the initial resting length between the particles by preventing them from moving too far apart or getting too close. The helical shape is achieved by having springs of varying resting lengths along the flagellum. The stiffness constants may also be different for each spring, and their values control the flexibility (elasticity) of the flagellum. Higher stiffness results in more rigid structures.

In our model, a particle may be connected by springs to several other particles. Therefore, the force at a particle may have several contributions from several springs. We use the sum of the forces at each point in the computation of the velocity as described below. A torque of constant magnitude and perpendicular to the base of the flagellum (see Section 4) is applied only at one point at the base of each flagellum to generate the rotation due to the motors. As the flagellum moves, the torque direction is adjusted so that it remains perpendicular to the base of the flagellum.

The motion of the flagella is computed as follows. Given the positions of all particles at time t, all forces $\mathbf{f}_j$ are computed based on the geometry of each flagellum. A torque $\mathbf{L}_i$ of a fixed magnitude is applied at the base of each flagellum in the direction perpendicular to the cross-section of the base. Once the forces and torques are known, the velocity at any location $\mathbf{x}_k$ is computed using the regularized Stokeslet and rotlet formula:

$$\frac{\mathrm{d}\mathbf{x}_k}{\mathrm{d}t} = \mathbf{u}(\mathbf{x}_k) = \sum_{i=1}^{N_r} \mathbf{U}_{\delta,r}(\mathbf{x}_k; \mathbf{y}_i, \mathbf{L}_i) + \sum_{j=1}^{N_s} \mathbf{U}_{\delta,s}(\mathbf{x}_k; \mathbf{z}_j, \mathbf{f}_j) \tag{8}$$

where N_r is the number of rotlets of strengths $\mathbf{L}_i$ located at $\mathbf{y}_i$ and N_s is the number of Stokeslets of strengths $\mathbf{f}_j$ located at $\mathbf{z}_j$. The expressions in this formula are given by Eqs. (5) and (6).

The position of each particle changes according to the fluid velocity so that each particle position can be updated after a small time interval. At that time, the new particle positions define new forces and new torques which are used for the next time step. In this way, the forces impose a time scale in the problem where the velocity of the particles is the superposition of the regularized Stokeslets and the rotlet. The time evolution of the particle positions is computed using a fourth-order Runge–Kutta method.

3.1. *Comments on the numerical method*

While the use of rotlets is new, the method of regularized Stokeslets, given by

$$\frac{\mathrm{d}\mathbf{x}_k}{\mathrm{d}t} = \mathbf{u}(\mathbf{x}_k) = \sum_{j=1}^{N_s} \mathbf{U}_{\delta,s}(\mathbf{x}_k; \mathbf{z}_j, \mathbf{f}_j),$$

has been used in two and three dimensions. The method can be used in two ways. The forward method consists of computing the velocity field due to given forces that are calculated from the geometry of the body, for example. The inverse problem consists of computing the forces (or the Stokeslets strengths) for the body to move with a prescribed velocity. The latter is necessary when the body's velocity is known in advance, and it requires the inversion of the Stokeslet operator. More details are found in Cortez (2001) and Cortez et al. (in press). This is the approach used in Lighthill (1976), Goto et al. (1999, 2001) and Ramia et al. (1993) because the geometry was known. In our case, changes in the geometry are part of the solution and so the motion is not known in advance.

In the current problem, the forces along the flagella are computed at every time step from Hooke's law based on their geometry. Then, the velocity field due to those forces (and the rotlets) is computed directly from Eq. (8). No operator needs to be inverted since the flagellar velocities are part of the computed solution, not a prescribed boundary condition. The method does not distinguish between a point on the body surface or a fluid marker at the same location. Since the body's velocity is computed using the same formula as the fluid velocity, the no-slip boundary condition is automatically satisfied. The fluid is dragged by the body as it moves. This is the same type of approach used by other methods (Dillon and Fauci, 2000; Peskin, 2002).

The analysis of the convergence of the method of regularized Stokeslets as the discretization is refined and the regularization parameter is reduced is found in Cortez et al. (in press). The main result is that the error in the velocity field near the body, as compared to a boundary integral formulation, is $O(\delta) + O(\Delta s^2/\delta^3)$, where Δs^2 is a discrete element of area on the body. The error decreases to $O(\delta^2) + O(\Delta s^2/\delta^3)$ away from the body. This allows one to choose the regularization parameter δ relative to the surface discretization in such a way that the method converges (for example, $\Delta s \sim \delta^2$).

4. A single flagellum

We present the model of a single flagellum without a body. In *E. coli*, each flagellum is shaped into a left-handed helix that extends from the cell body. Our goal is to create a solid, yet flexible, representation of the flagellum. We define the flagellum to be a helical tube of total length ℓ with cross-sections perpendicular to the tangent vector (see Fig. 2). Each cross-section is an n-sided polygon. The helix has a varying radius, $R(s)$, which is implemented using an arctangent envelope that allows the radius to start from zero and increase to some fixed value. This is similar to the envelope used in Higdon (1979b) and Ramia et al. (1993). The initial conditions for the particles are as follows:

$$\begin{aligned} x(s) &= \alpha(s) \\ y(s) &= -R(s)\cos\left(2\pi n_p\left(\frac{s}{\ell}\right)\right) \\ z(s) &= R(s)\sin\left(2\pi n_p\left(\frac{s}{\ell}\right)\right) \end{aligned}$$

where the amplitude $R(s)$ satisfies $0 \le R(s) \le R_h$ and is given by

$$R(s) = R_h\left[\frac{1}{\pi}\arctan\left(\beta\left(\frac{s}{\ell} - \gamma\right)\right) + \frac{1}{2}\right],$$

n_p represents the number of turns in a helix, and $\alpha(s)$ is found so the tangent vector $[x'(s), y'(s), z'(s)]$ has unit length. We emphasize that the shape of the flagellum for $t > 0$ is not specified but found as part of the computation. The benefit of the arctangent envelope is that it defines an axis of rotation at the base of the flagellum while creating a helix of

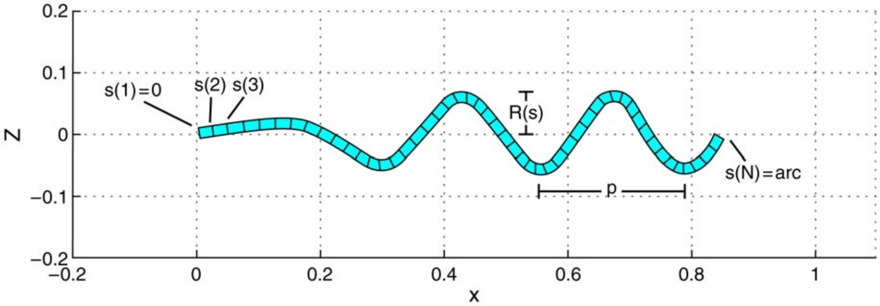

Fig. 2. Side view of one helical flagellum.

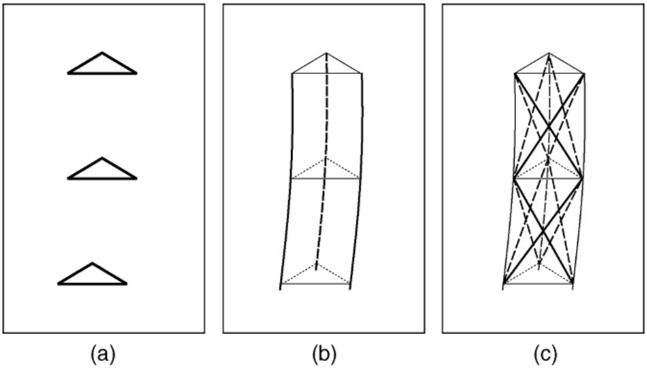

Fig. 3. Spring connections: (a) cross-sectional springs; (b) consecutive springs; (c) diagonal springs.

constant radius in the rear as can be seen in Fig. 2. For economy of computation, we choose $n = 3$ for the cross-sections, the smallest number possible, so that each flagellum is a structure made of 3 helices defining triangular cross-sections. This choice, however, is not a restriction.

In Fig. 3, we show the spring connections that are defined between different particles. First, each particle on a helix is connected to the corresponding particles on the other two helices [Fig. 3(a)]. This defines the cross-sections of the flagellum and will be referred to as *cross-sectional forces* with stiffness constants of k_a. Next, each point on a helix is connected to adjacent points on the same helix using spring forces; this is shown in Fig. 3(b). These will be referred to as *consecutive forces* with stiffness constants k_b. We also define diagonal forces around the surface of the flagellum. The bold lines are the *diagonal forces* with stiffness constants k_c [Fig. 3(c)]. We note that these stiffness constants actually have units of force density as defined in Eq. (7). However, since the resting lengths of the springs (L_0^{jk}) will remain constant throughout the simulations, the parameters (k_a, k_b, k_c) are appropriate.

A biological flagellum is a helical tube composed of flagellin monomers arranged in a pseudohexagonal lattice (Jones and Aizawa, 1991). Some monomer strands

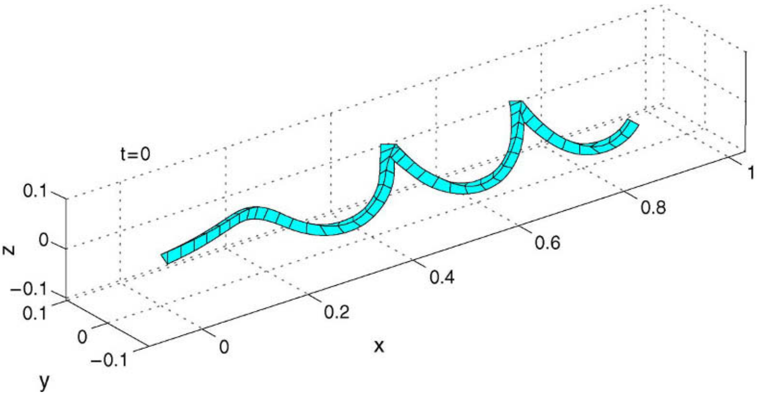

Fig. 4. Initial configuration of a single flagellum.

(protofilaments) are nearly parallel to the filament axis while others (so called 5-start and 6-start) form helices along the surface of the flagellum. The latter are represented by the diagonal springs in our model and the protofilaments are represented by the consecutive springs. The number of particles used in the construction of our model has been reduced for computational purposes only, but this is not essential. Our structure has the benefit of being composed entirely of triangles. Triangles, unlike other polygons, have the property that they preserve angles when preserving the length of the sides. A slight modification of our model can be made to represent the flagellin monomers as depicted in Fig. 6 of Jones and Aizawa (1991). This has been done recently in Lim and Peskin (2004) to address whirling instabilities of some elastic filaments.

The external torque is positioned at the center of the first cross-section of the flagellum (see also Fig. 9). Because of the varying helix amplitude, the first cross-section is perpendicular to the central axis of the helical flagellum. This makes it appropriate to define the torque orthogonal to the first cross-section. We note that since the torque is imposed externally to simulate the motor, the net torque will not be zero.

Fig. 4 shows the initial conditions for this problem. Since the flow due to the rotlet decays as r^{-2} for large values of r, nearby cross-sections experience more rotation than ones far from the rotlet. The distances between contiguous cross-sections deviate from their resting-lengths due to the rotation. This is particularly pronounced near the front of the flagellum. In response to the stretching, the springs exert forces that pull the rest of the flagellum, making the entire structure rotate. The diagonal forces are essential in this process since they have a significant effect on propagating rotation along the entire flagellum. They also affect the amount of twist developed along the flagellum.

4.1. Parameter dependence of a single flagellum

The motion of a single flagellum is induced by a torque applied at its base. The parameters were chosen so that the flagellum held together in its helical form while still allowing it to rotate with some elasticity. The rotation of the entire structure in a viscous fluid necessarily results in forward swimming motion of the flagellum. In this section,

Table 2
Comparison of forward swimming speed as a function of the spring stiffness

k_a, k_b, k_c	Dimensionless speed, v ($\times 10^{-4}$)	Speed $= Uv$, (μm s^{-1})
4, 4, 4	1.2272	12.272
8, 8, 8	1.2245	12.245
12, 12, 12	1.2219	12.219
16, 16, 16	1.2204	12.204

The dimensionless parameters used were $\delta_s = \delta_r = 0.052$, $L = 0.001$, $n_p = 3$, $p = 0.2399$, $\ell = 1.3$.

we discuss the effect of some parameters in the model on the swimming speed and angular speed of the flagellum. In most of the numerical experiments, the flagellum length was fixed at $\ell = 1.3$ (equivalent to 13 μm). In all numerical experiments, the maximum helix radius was fixed to $R_h = 0.06$, which is about 5% of the flagellum length. The radius of the flagellum was fixed to a value of 0.012, which is about 1% of the flagellum length. This corresponds to a somewhat thick flagellum of 120 nm in radius, which is thicker than a typical *E. coli* flagellum (Turner et al., 2000). Alternatively, one may assume that the computational flagellum is short for its thickness. Experimental studies also have been conducted on flagellar models which have a small length-to-radius ratio (Kim et al., 2003). We present other computational experiments which use longer flagella as indicated in Table 5. Based on numerical experiments, most of the reported results use $N = 51$ cross-sections to discretize the flagellum since larger numbers of cross-sections had no significant effect on forward motion or stretching.

In a computational flagellum, there are many different parameters that affect its motion. To analyze the effect of one parameter, we monitored the angular velocity, forward displacement, and structural stability. Here we discuss the changes caused by varying the stiffness constant values (k_a, k_b, k_c), the regularization parameters for both the Stokeslet (δ_s) and the rotlet (δ_r), the magnitude of torque applied (L), number of periods in a flagellum (n_p), pitch (p), and arclength (ℓ). All computations in this section were run up to a final dimensionless time of 400, corresponding to $t = 0.04$ s. The linear speed of the flagellum was computed from its final and initial positions.

The **spring constants** must be set to large enough values in order to maintain the helical shape of the flagellum. Once the spring constants are sufficiently large, they have little effect on the structure of the flagellum and forward motion. As can be seen in Table 2, for the range of spring constant values chosen for the parameter analysis, variations have little effect on forward motion. Although at smaller constant values, there is slightly more stretching of the flagellum. For these reasons, the stiffness constants were set equal to 12 for all computations in this section.

The regularization parameters for the Stokeslet and the rotlet are independent of one another. These were set to a multiple of the distance between the cross-sections in the flagellum. For N cross-sections along the helix of length ℓ, this distance is $\ell/(N-1)$. For the tests in Tables 2, 3 and 5, this cross-sectional distance was 0.026. Changing the **Stokeslet's parameter** δ_s has contrasting effects on forward motion and the stretching of the flagellum. The value of δ_s should be comparable to the separation between cross-sections along the flagellum so that the cutoff functions of nearby forces can overlap.

Table 3
Effect of the Stokeslet regularization parameter δ_s on the swimming speed and filament stretching

δ_s	Speed (μm s^{-1})	Stretching (% of ℓ)
0.026	7.692	0.23
0.052	12.219	0.77
0.078	14.522	2.31

The dimensionless parameters used were $\ell = 1.3$, $\delta_r = 0.0526$, $L = 0.001$, $n_p = 3$, $p = 0.2399$.

This is needed for accuracy purposes (Cortez et al., in press). Our results, shown in Table 3, show that larger values of δ_s yielded faster forward motion but also produced more stretching. This is to be expected since larger values of δ_s produce forces that are spread over larger regions and reduce the maximum value of the cutoff function being used. This produces smaller reaction forces by the springs and allows more stretching.

The torque magnitude L and the **rotlet regularization parameter** δ_r have a large effect on forward motion and the structure of the flagellum. We varied the amount of torque applied and studied its effect on forward motion and angular velocity. Physical experiments performed by Purcell (1997) assumed linear relationships between the torque magnitude and the axial angular speed, and between the swimming speed and angular speed, consistent with Stokes flow. He expressed these relationships with the scalar equations

$$F = Av + B\omega, \tag{9}$$

$$L = Cv + D\omega, \tag{10}$$

where F is the net applied external force magnitude, v is swimming speed, ω is the angular speed, L is the net torque magnitude, and A, B, C, and D are constants that depend on the geometry of the flagellum. These equations reflect the relationships in the direction of the axis of the flagellum under the assumption that the other components average to zero as the flagellum corkscrews its way through the fluid. There is no net external force in our system, so $F = 0$ in Eq. (9) and the correspondence between v and ω is a line through the origin. This, together with Eq. (10), results in a linear relation between ω and the net torque, and also between v and the net torque. We computed the flagellar motion for a wide range of torque magnitudes L and verified that our model produces a linear relation between the swimming speed v and ω, between the torque magnitude L and ω, and therefore, between the torque magnitude and the swimming speed (see Fig. 5). The linear relationships hold for different values of δ_r. Eq. (6) indicates that the rotlet velocity can be written as $\mathbf{U}_{\delta,r}(\mathbf{x}; \mathbf{x}_0, \mathbf{L}_0) = \delta_r^{-2}\mathbf{U}_{\delta,r}(\mathbf{x}/\delta; \mathbf{x}_0/\delta, \mathbf{L}_0)$ so that as δ_r is reduced, the torque is concentrated in a smaller region and its maximum value increases, resulting in faster rotation.

The **number of periods**, n_p, in the helix comprising each flagellum also has an effect on both its swimming motion and its ability to hold its shape. We report results using four, three and two helical periods while keeping the pitch p constant. Since flagella with more periods of a given pitch are longer than those with fewer periods, one expects that for a given driving torque, the viscous drag would have a larger effect on a flagellum with

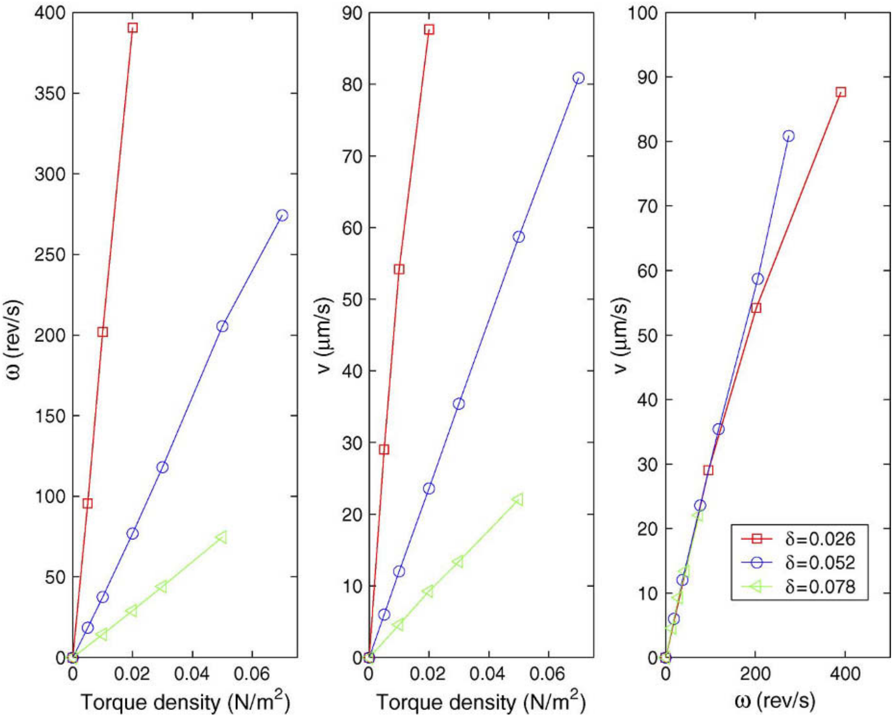

Fig. 5. Magnitude of torque density L vs. angular speed ω (left); magnitude of torque density L vs. linear swimming speed v (middle); angular speed ω vs. swimming speed v (right).

Table 4
Comparison of the forward swimming speed and angular speed of a flagellum with constant pitch as a function of the number of helical periods along its length

n_p	ℓ (μm)	N	Speed (μm s^{-1})	ω (rev s^{-1})
2	8.7	34	17.0	20
3	13.0	51	12.2	15
4	17.3	68	9.6	10

The driving torque was fixed with magnitude $L = 0.001$. The dimensionless parameters used were $\delta_s = \delta_r = 0.052$, and pitch $p = 0.24$.

more periods causing a smaller angular velocity and, therefore, slower swimming motion. Our results, shown in Table 4, show that having fewer periods causes less stretching and resulted in faster swimming, as expected. For this experiment, the number of cross-sections along the flagellum was increased as the number of periods increased in order to maintain a constant cross-sectional spacing.

The **pitch** of the flagellum has almost no effect on ω for a rotlet of fixed magnitude. The pitch was varied by fixing the flagellum length and changing the number of turns in the helix. Having more or fewer turns per arclength did not have an effect on the angular

Table 5
Comparison of speed as a function of pitch for flagella of different lengths and different number of helical periods

ℓ (μm)	N	n_p	Pitch (μm)	ω (rev s^{-1})	Speed (μm s^{-1})
17	51	2	7.61	100	37.0
17	51	3	4.36	100	40.6
17	51	3.5	3.20	100	34.7
17	51	4	2.28	100	24.6
25	75	2	11.68	70	19.5
25	75	3	7.47	70	27.9
25	75	4	5.12	70	30.7
25	75	4.5	4.22	70	29.4

The dimensionless parameters used were $\delta_s = \delta_r = 0.052$, and $L = 0.005$.

velocity ω. However, the model shows that the maximum swimming speed is achieved for a given pitch which is not particularly sensitive to arclength. Intuitively, if the pitch is very large, the flagellum is nearly a straight tube and does not swim efficiently. On the other hand, if the pitch is very small, the helix is tightly wound and the flagellum does not swim efficiently either. Thus, one expects a selected pitch to yield a maximum swimming speed [see also Cortez et al. (in press)]. Table 5 shows the results for flagella of fixed length and variable number of turns (different pitch). This was done with two different arclengths while maintaining the same cross-sectional distance. We define the optimal pitch to be the one that yields the largest swimming speed. Based on the results we estimate the optimal pitch to be about 4.5–5 μm. For comparison, we mention that pitch measurements of stationary normal flagellar filaments found in Turner et al. (2000) and Kim et al. (2003) are in the range 1–3 μm.

4.2. *Flow generated by a flagellum*

The motion of the flagellum generates fluid flow around it. Two-dimensional projections of the fluid flow on planes perpendicular to the axis of the flagellum are shown in Fig. 6. The triangle in each plot is the projection of a flagellum cross-section. The top-left plot shows the first cross-section, where the torque is applied. The flow here is largely dominated by the torque. Further back along the flagellum, as the effect of the torque decays, the flow is influenced more substantially by the spring forces that cause the flagellum cross-sections to rotate in circles. Fig. 7 shows the flow projected onto a plane that includes the flagellum axis. The top plot is the initial position of the flagellum and the bottom plot shows the flagellum and the flow around it at $t = 0.02$ s. The forward motion of the flagellum is apparent and is also indicated by the fluid motion since there is flow coincident with the helix tangent. The figure also shows regions of fluid rotation in alternating directions that approximately coincide with the helix shape.

5. Three flagellum model

In this section, we discuss the interactions among three flagella through the fluid flow they generate. In particular, we are interested in the role of the fluid motion in the processes

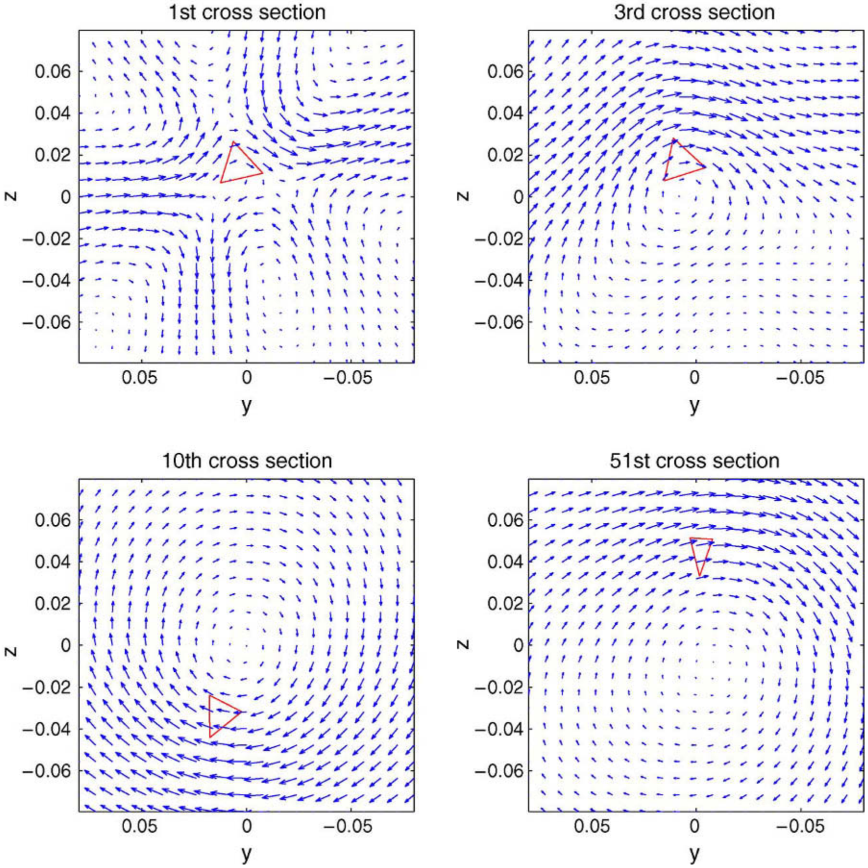

Fig. 6. Flow fields at the 1st, 3rd, 10th, and 51st (last) cross-sections of a flagellum.

of bundling and tumbling. Our model includes three flagella constructed in the same way as described in the previous sections. Each one has a motor modeled by a torque in the center of the first cross-section. While we do not construct explicitly the body of the organism, the model includes features related to the effects of the bacterial body on the motion. The three flagella were placed equally-spaced around a circle whose radius represents the radius of the bacterial body. To simulate the front of these flagella being connected to a rigid body and not being able to freely change their distances and orientation relative to one another, the front sections of the flagella were connected by springs. These springs connect the center points of the first three cross-sections of each flagellum with the corresponding cross-sections of the other two flagella. Fig. 8 shows these connections. Under this construction the center points of the first cross-sections of the three flagella form an equilateral triangle and remain at approximately the same distance throughout the simulation.

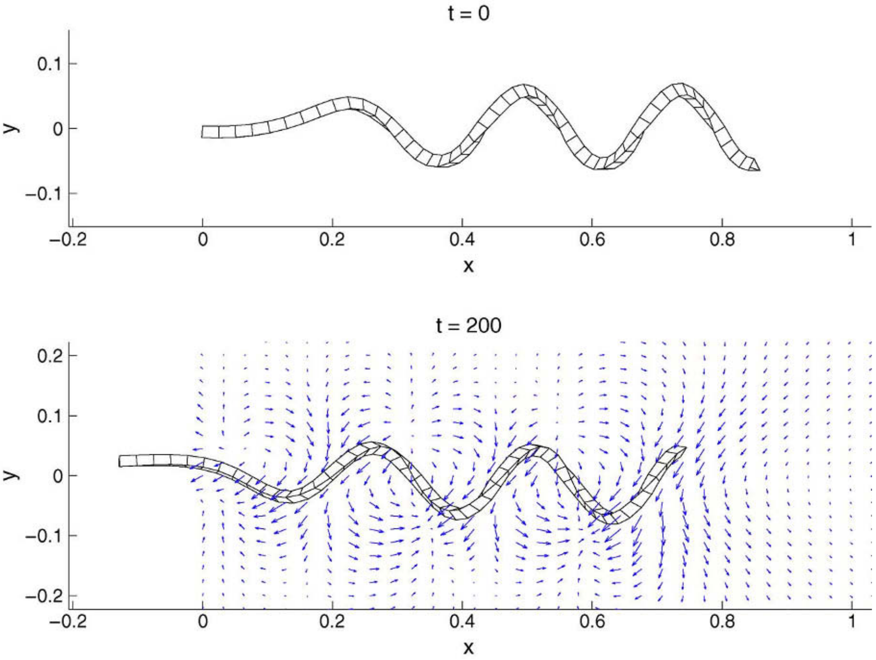

Fig. 7. Initial position and flow field through a middle plane in the flagellum at dimensionless time $t = 0.02$ s.

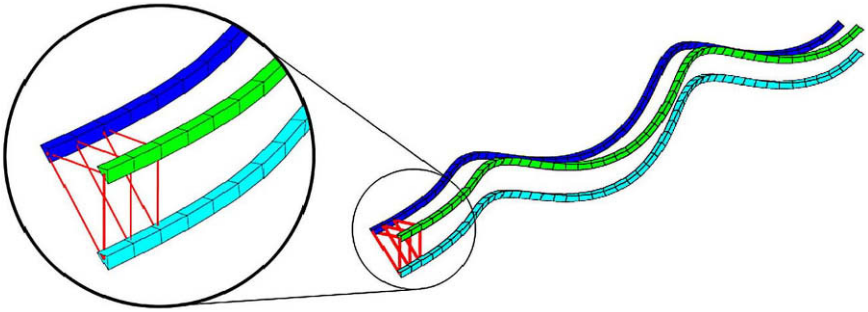

Fig. 8. View of initial conditions for the three-flagellum case.

Since the representation of the flagella in our model is by discrete points, there is a possibility that in the computation they may get closer than physically possible. We prevent two flagella from crossing each other by defining repulsive forces which are turned off when the flagella are apart. We define the minimum distance between the centerlines of different flagella before they come into physical contact with one another, and set this distance as the threshold for activation of the repulsive forces. Physically, the distance between two flagellar centerlines must be no smaller than the diameter of the flagellum. In the remaining computations, we use the slightly larger activation threshold of 2.3 times the

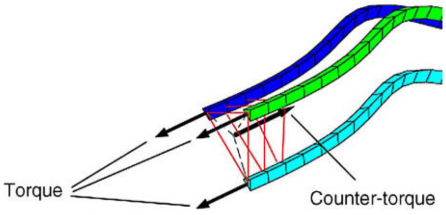

Fig. 9. Torque setup for the three-flagellum case.

flagellar radius. This choice was made purely for computational purposes since the fluid flow between the flagella is not well-resolved at those distances for the discretization used.

The torques located at the base of each flagellum generate rotation throughout the fluid. Since we are interested in the flagellar interaction due to the fluid motion and not due to the flagella revolving around one another, we introduce a *counter-torque* to represent the counter rotation effect of the bacterial body. This counter-torque is in the opposite direction of the three motor torques and is designed to keep the bases of the flagella from revolving around each other. In this way, the bundling observed would be a direct result of the hydrodynamic interactions. The counter-torque is placed at the center of the triangle defined by the center points of the first cross sections of the three flagella, so that it is equidistant from the other three torques located at the vertices of the triangle. Its direction is perpendicular to the plane of the triangle and pointing in the opposite direction of the other three torques; see Fig. 9.

We compute the magnitude of the counter-torque dynamically at every time step to cancel the rotation of the front flagellar cross-sections (where the motors are located) around each other. This was accomplished by computing first the velocities of these cross-sections due to all the forces and motor torques and projecting these velocities onto the circle defined by the location of the motors. The magnitude of the counter-torque was computed to cancel the average projected velocity.

This definition of the counter-torque leads to simulations in a reference frame in which the bacterial body does not rotate. This case is similar to a laboratory setup in which each flagellum is connected at the base to an stationary motor which does not allow it to spin around the other flagella (Kim et al., 2003). This is not unrealistic on a time scale of a few flagellar rotations since the bacterial body of *E. coli* rotates with a frequency of 10 rev s^{-1} (see Powers, 2002) whereas the flagella rotate with a frequency of 100 rev s^{-1} (see Berg, 2003). Powers (2002) discusses the possibility of bundling by spinning one end of a flexible filament (similar to body rotation) and determining possible steady-state configurations. In the present study, the goal is to uncover the role of the hydrodynamic interactions that lead to bundling and not the mechanical turning of one flagellum around another. For this reason we work in this reference frame. We expect to learn the flow interactions among the flagella from the analysis of this experiment. In this frame, the angular momentum will be conserved only approximately and the net torque will not be exactly zero. It is possible to adjust the location of the counter-torque in order to minimize the net torque, however this was not done here.

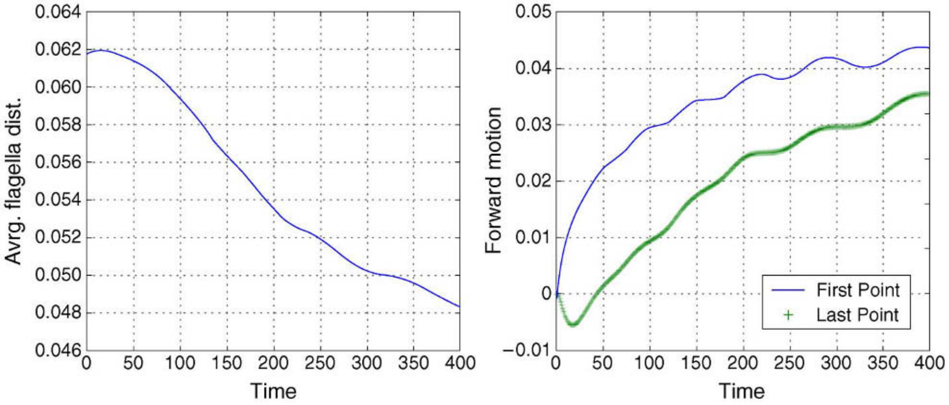

Fig. 10. Plot of average distance between flagella (left) and forward displacement of the front and last cross-sections (right). The difference between the latter represents stretching of the flagellum.

Table 6
Table of parameter values used for the results shown in Fig. 11

Parameter	Dimensionless value	Dimensional value
Number of cross-sections	51	51
Flagellum radius	0.01	0.1 μm
Helix radius (R_h)	0.06	0.6 μm
Arclength of flagellum	1.3	13 μm
Number of periods	2	2
Initial flagellar separation	0.05	0.5 μm
k_a, k_b, k_c	10	10^7 N m^{-3}
δ_s	0.039	0.39 μm
δ_r	0.052	0.52 μm
Magnitude of torque (density)	0.002	0.02 N m^{-2}

5.1. Bundling of three flagella

One important feature of bundling is how close the flagella get to one another. In order to characterize the distance between the flagella, we computed and monitored the distances between the centers of the cross-sections. We first defined the distance between one cross-section of a flagellum to another flagellum to be the minimum distance between the center of the cross-section and the center of all the cross-sections of the other flagellum. By computing the minimum, maximum and average of these distances, one can monitor the average separation between flagella. Fig. 10 shows the average distance between flagella for the case analyzed in the next section (see Table 6). This average distance decreases substantially in time as the flagella start to bundle.

Another property that we examined was the forward displacement of the flagella. This was measured by comparing the position of the center of the first cross-section of the three flagella and their corresponding initial positions. Similarly, we computed the corresponding

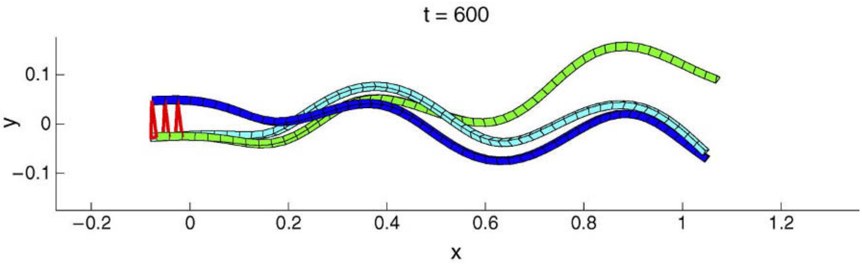

Fig. 11. Side view of the flagella at $t = 0.06$ s using zero angle of incline and $k_a = k_b = k_c = 10$.

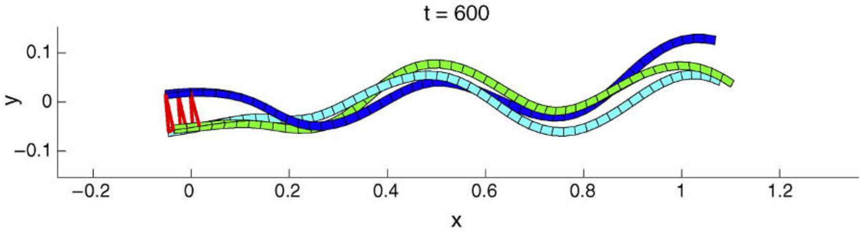

Fig. 12. Side view of the flagella at $t = 0.06$ s with angle of incline 1.2° and $k_a = k_b = k_c = 10$.

quantity at the last cross-section. The two curves are shown in Fig. 10. The gap between these curves represents stretching which is caused by the elasticity of the flagella. Notice that most of the stretching occurs early in the motion. The slope of the curve gives the swimming speed of the flagella. As the flagella get closer together, the computation of the motion becomes more demanding in order to prevent the numerical crossing of any two flagella. Consequently, the time step in the computation must be reduced, making a long-time simulation challenging.

Fig. 11 shows the final snapshot at $t = 0.06$ s of the simulation using the parameters given in Table 6. The figure shows that the front half of the flagella form a tighter bundle than the back of them. This was typical of our simulations. We found, however, that the stiffness parameters and the initial conditions are factors that can affect the tightness of the bundle. The free ends of the flagella come closer together at the end of the simulation if the initial conditions are modified slightly in such a way that the helix axes are not parallel but tilted by just 1°–2° so that they are barely closer at the tails than at the front. This modification appears to be enough for all the cross-sections of the flagella to spiral toward a bundle. Fig. 12 shows a simulation using the parameters of Table 6 and an angle of incline of 1.2°. Note the tighter bundle along the entire flagella.

The stiffnesses of the springs also have an effect on the bundle. Fig. 11 shows a snapshot of the simulation in which the stiffness constants were set to $k_a = k_b = k_c = 10$ (dimensionless units). Recall that k_a corresponds to springs connecting the points on a single cross-section; thus, these springs are responsible for maintaining the integrity of the tubular flagellum. The stiffness constants k_b correspond to springs connecting contiguous cross-sections along the axis of the flagellum and the diagonal springs correspond to k_c.

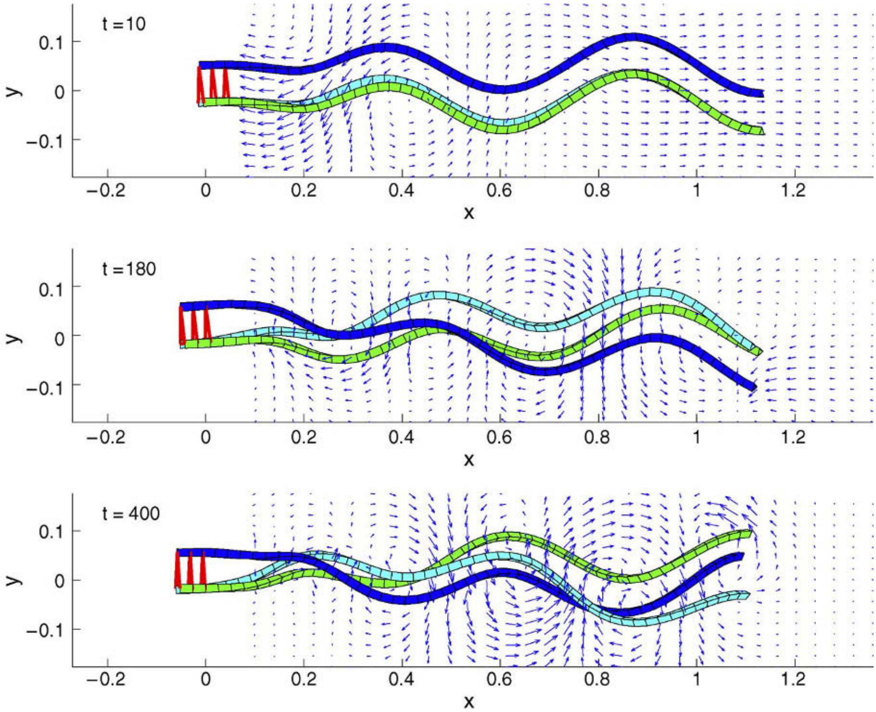

Fig. 13. Side view of the flagella at three different times with $k_a = 10$, $k_b = k_c = 4$.

These two types of springs give flexibility to the flagellum in terms of its ability to bend and twist. Reducing the values of these stiffnesses makes the flagella more malleable and can affect their ability to form a bundle. In Fig. 13, we used the values $k_a = 10$ and $k_b = k_c = 4$. The tail end of the flagella are closer and the flow around it resembles the flow around a single flagellum (compare to Fig. 16). This may indicate a better propulsion configuration. It is also apparent that the flagella are tangled more. Further reducing the stiffnesses to $k_a = 10$, $k_b = k_c = 2$ (not shown) allows the flagella to bundle even more but the helical shape begins to straighten out because the springs are too weak to maintain that shape.

The amount of twist in the flagella at the end of the simulation is also larger with the reduced stiffnesses. We calculated the twist from front to back of the flagella shown in Fig. 11 to be 1.49 rad while the twist in the bottom plot of Fig. 13 was 4.14 rad. The twist in the flagella that uses $k_b = k_c = 2$ was 7.53 rad, indicating that the spring construction allows for changes in the elastic properties of the flagella. In fact, each spring can be made to have its own stiffness constant.

5.2. *Flow generated by three flagella*

Our numerical experiments indicate that the process of bundling can be accelerated by placing at least the tail ends of the flagella slightly closer, as explained in the previous

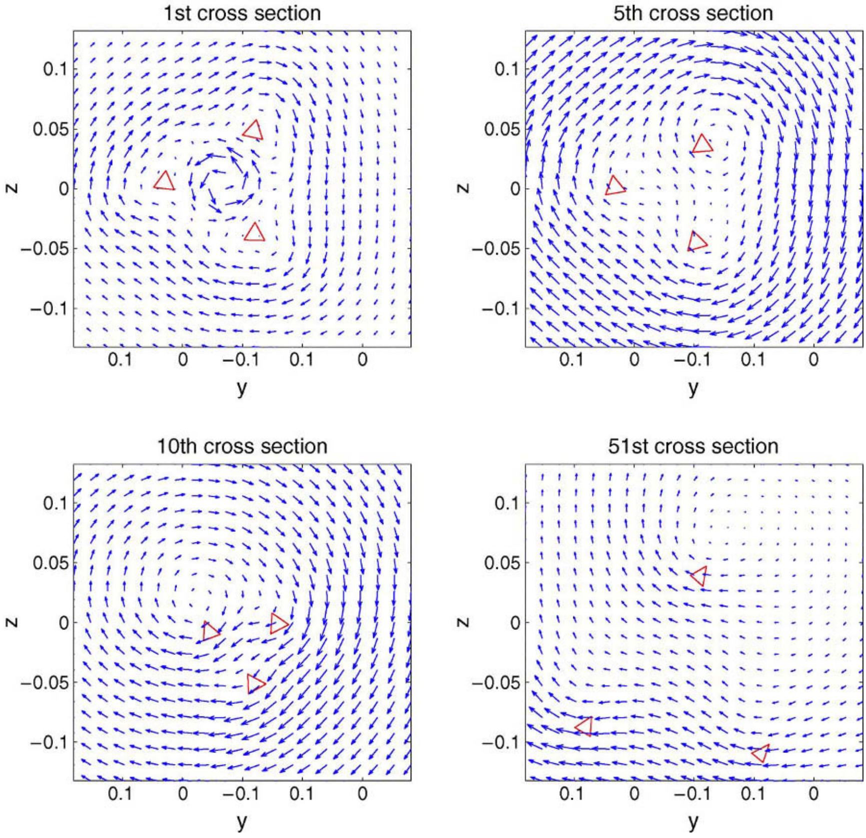
1st cross section

5th cross section

10th cross section

51st cross section

Fig. 14. Cross-sectional view of fluid flow near the three flagella ($t = 0.04$ s). The plots show the flow on planes at the front, back and two intermediate locations along the flagella.

section. In the experiments of this section, we present results using the parameters given in Table 6 and an angle of incline of 1.2°. The only purpose of this is to reach a bundled state earlier in the simulation. The parameter values fall within the range computed for the single flagellum for favorable swimming speed.

We focus on the fluid flow around the flagella. The flow generated by the three flagella has a different character depending on the distance from the torques. The flow near the first cross-sections of the flagella is mainly dominated by the effect of the torques; see the top-left plot in Fig. 14. At this location, which is the plane where the torques are located, the forces act to keep the cross-sections from deforming and to maintain their relative distances approximately constant. One can see the effect of the counter-torque at the center of the graph.

Further away, the torques generate a more uniform single rotation. The effect of the torques also decreases as the distance from the torques increases, and the effect of the forces along nearby cross-sections becomes more significant. For the particular results

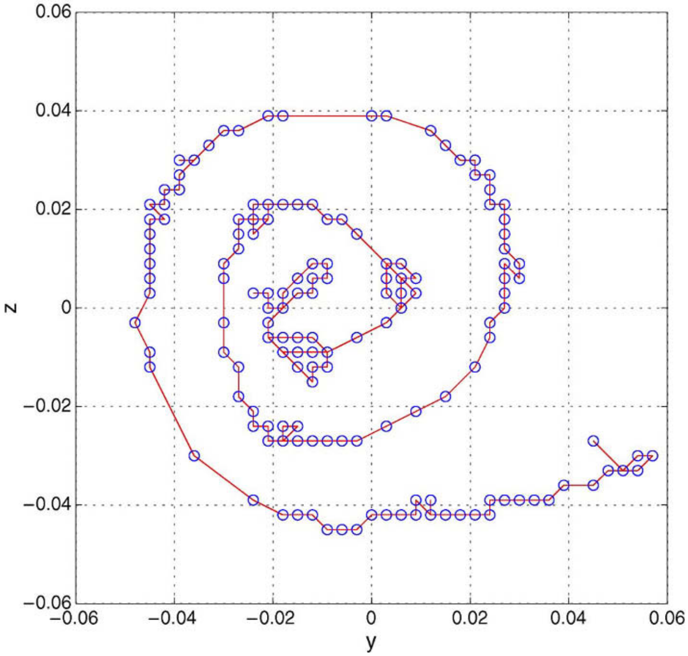

Fig. 15. Position of the center of fluid rotation on a plane perpendicular to the flagellar axis at the 15th cross-section as a function of time. The center of fluid rotation starts on the right side and spirals inward in time promoting bundling.

displayed in Fig. 14, the flow beyond a quarter length of the flagella is dominated by the forces (Stokeslets) while the torques (rotlets) have little effect. The top-right plot shows the flow near the front but far enough away from the torques that there is a single center of rotation (where the flow is zero in the plot) between the three cross-sections. The bottom-left plot in Fig. 14 shows how the rotation is altered by the effect of the forces in the regions close to the flagella. The center of rotation is no longer on the center axis of the three flagella and the resulting flow pulls the flagella located furthest away from the center of rotation toward the other flagella. We point out that the flagella can be seen to be very close to one another in the bottom-left plot of Fig. 14. The bottom-right plot shows the flow at the tail. For all the observed time, the cross-section located furthest away from the center of rotation was always pulled in its direction. This type of flow, in turn, promotes bundling.

Fig. 15 shows the location of the center of rotation of the fluid about a quarter length of the flagella from the front. The points shown are not part of any flagella but are points in the fluid where the flow is zero. As time increases, the center of fluid rotation moves in a spiral pattern causing the flagella to come together during bundling.

By analyzing the flow on the xy-plane (see Fig. 16) we observe the appearance of regions of circulation. This flow is an expected result from the motion of the flagella (Gray, 1968; Lighthill, 1976). The direction of the flow rotation changes when the concavity of

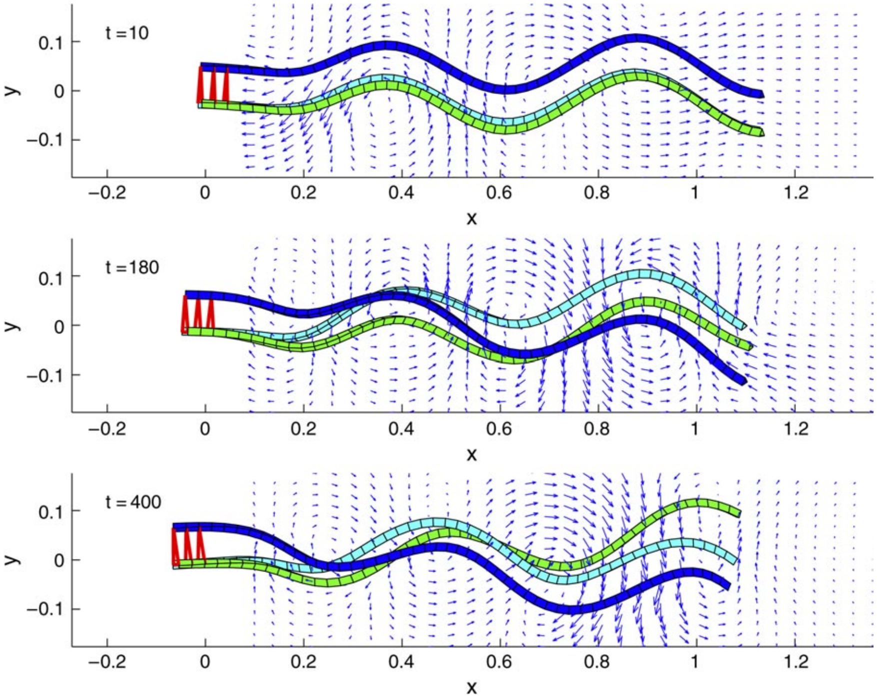

Fig. 16. Side view of the flagella and the fluid flow around them at three different times of the simulation $k_a = k_b = k_c = 10$.

the helix changes as viewed from the side. These side views of the flow also make evident the end-effect of the flagella. The force balance at the end of the flagella is different from the balance in the middle and this affects the flow. One can also compare this plot with Fig. 13 to notice that the small angle of incline used in the latter does speed up the bundling process. With the small tilt of the helix axes, the flagella wrap around one another for about half the total length after the same final simulation time. We point out that the same phenomenon where parts of the flagella come close to one another while other sections remain apart has also been observed experimentally (Kim et al., 2003).

For comparison with the numerical simulations of the next section, we show in Fig. 17 four snapshots of the flagella entering into the bundle. The parameters used here are those in Table 7 with all motors rotating counterclockwise when viewed from behind the flagella. Note that the torque magnitude is larger than in the previous simulations, and therefore the final simulation time is shorter. In the simulation time shown in this figure, the average distance between the flagella decreases from 0.867 to 0.653 μm and continues to decrease in time. It is also clear from the figure that the orientation of the flagella remains the same throughout the simulation. The total time of this simulation is $t = 0.0135$ s, which is sufficient to show the onset of the bundling process. The forward displacement of the flagella, however, is very small in this time scale.

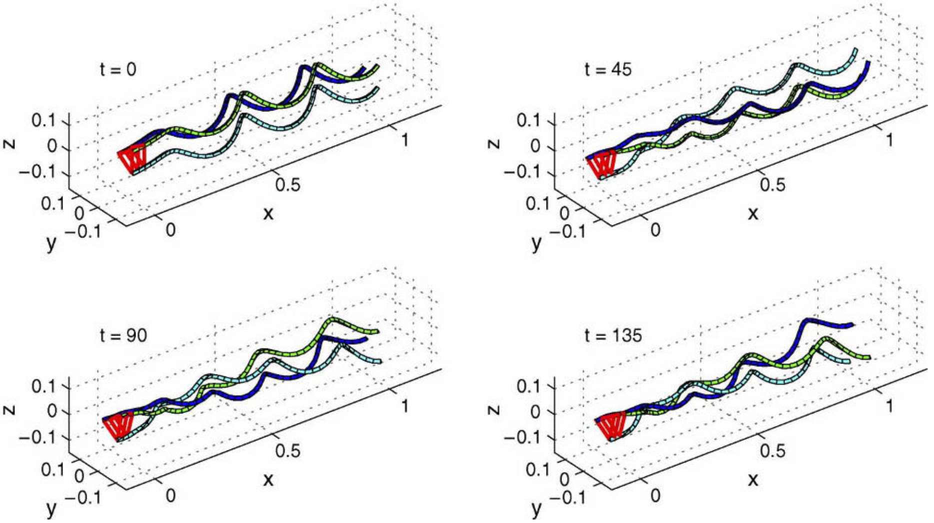

Fig. 17. Snapshots of the flagella entering into a bundle.

Table 7
Table of parameter values used for three-flagellum case in Figs. 17 and 18

Parameter	Dimensionless value	Dimensional value
Number of cross-sections	51	51
Flagellum radius	0.008	0.08 μm
Helix radius (R_h)	0.05	0.5 μm
Arclength of flagellum	1.3	13 μm
Number of periods	3	3
Initial flagellar separation	0.05	0.5 μm
k_a, k_b	10	1.0×10^7 N m^{-3}
k_c	12	1.2×10^7 N m^{-3}
δ_s	0.039	0.39 μm
δ_r	0.052	0.52 μm
Magnitude of torque	0.008	0.08 N m^{-2}
Angle of incline	0.0	0.0

5.3. *Results on tumbling*

In this section we test whether the same construction that produced bundling can produce tumbling. Tumbling occurs when one or more of the motors of a left-handed helix change their direction to a clockwise rotation (viewed from behind the flagella). When this occurs in laboratory experiments, the flagella are observed to behave erratically and the organism changes its orientation in apparently random fashion (Turner et al., 2000). We look at the case in which all the parameters and initial conditions are as in the previous section except that we change the direction of rotation of only one of the motors.

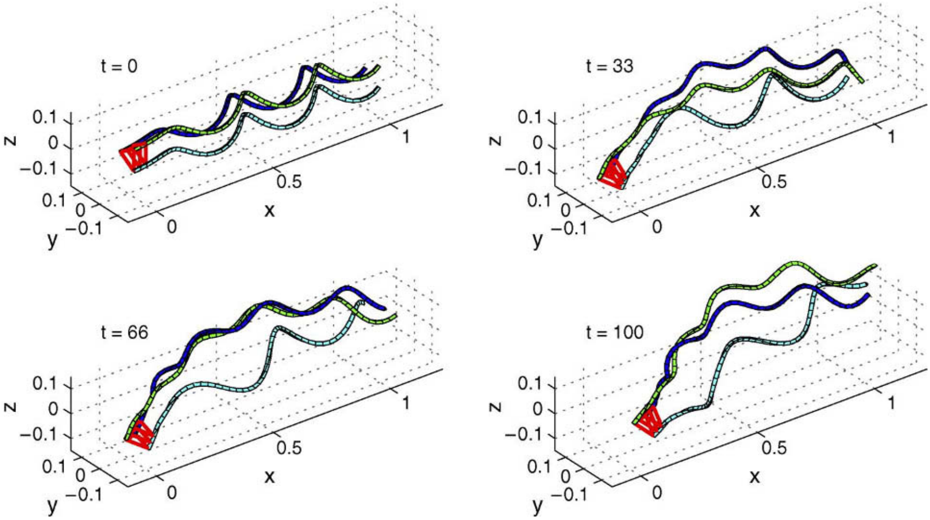

Fig. 18. Snapshots of the flagella entering into a tumble.

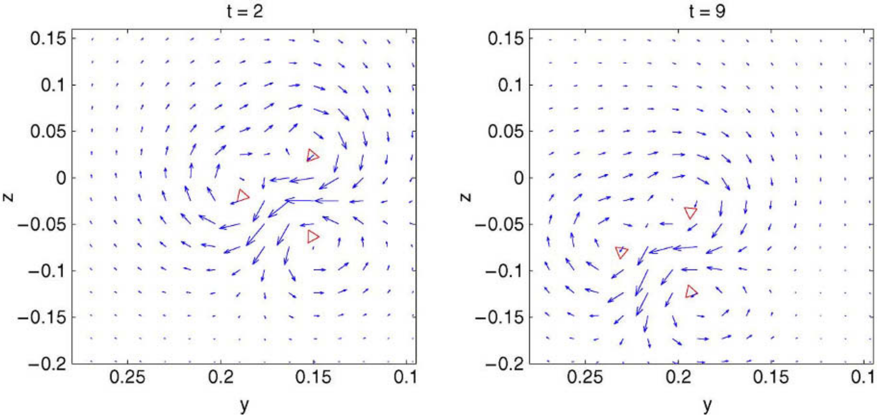

Fig. 19. The 1st cross section during the beginning of the tumble.

We use the parameters shown in Table 7 throughout this section. The same parameters were used for the results on bundling shown in Fig. 17 (compare the top-left plot of each figure). The only difference is that the sign of one of the rotlets was reversed to model the change in a motor rotation. We also ran the experiment reversing the rotation of two motors and the results are qualitatively similar to the ones shown here.

The resulting motion is depicted in Fig. 18 and should be compared with Fig. 17. Notice that although only the direction of rotation of one motor was changed, the motion is dramatically different from that in Fig. 17. Instead of getting closer and wrapping around one another, the flagella move away from one another and they change orientation.

In the span of 0.01 s, the maximum distance between the flagella increases from 0.867 to 3.305 μm, and the average distance between flagella increases from 0.867 to 1.285 μm. This also gives an indication that the tumbling occurs faster than bundling. In *E. coli* the bundling time is about ten times longer than the tumbling time (Turner et al., 2000).

The changes in orientation are also clear from Fig. 18 and it becomes more and more drastic as time progresses. The axial position of the tail does not change. This indicates that there is no net forward motion, but only a rotation of the flagella that changes their orientation.

When analyzing the fluid flow generated by the flagella, one can get an idea of how the change in the direction of rotation of some motors may cause tumbling. In Fig. 19, the flagellum in the lower right rotates counterclockwise while the other flagella rotate clockwise. This creates regions of counter-rotation in the fluid, which force the base of the flagella to change its orientation significantly since the cross-sections near the front of the flagella are at a fixed distance from one another and cannot separate. Except for the front few sections of the flagella, which are tied together, the rest of the flagella are free to move independently as they are carried by the flow. The counter-rotating flow regions created by the rotation of the motors in different directions generate fluid motion that separates the flagella along their lengths. Fig. 20 shows snapshots of a cross-section about halfway along the flagellar length and clearly shows the process of separation.

While the results in Figs. 17 and 18 show the effect of reversing the rotation of one motor starting from the same initial conditions, we are also interested in a longer simulation in which the motors reverse rotation in the middle of the motion. We set up an experiment consisting of three time intervals. First, all three motors rotate in the same direction for $0 \leq t < 0.0135$ s. This produces the bundling behavior shown in Fig. 17. At the final time, the sign of one of the rotlets is reversed during $0.0135 \leq t < 0.0270$ s. This produces a tumble shown in Fig. 21. Notice that the orientation of the flagella changes drastically and they separate. Finally, the motors again are set to rotate in the same direction as in the beginning of the simulation for the interval $0.0270 \leq t \leq 0.0405$ s as shown in Fig. 22. Notice that the flagella come together again into a tight bundle and now the orientation remains constant. We believe that the time intervals in the simulation are sufficient to initiate the bundling process or to move erratically during a tumble. However, the time intervals are not long enough to appreciate significant forward displacement during bundling.

6. Conclusions

A computational model of the interaction of multiple bacterial flagella was presented. The method of regularized Stokeslets is based on the superposition of exact solutions of the Stokes equations with external force given by a linear combination of cutoff functions. These functions concentrate a given force in a small sphere rather than at a point, as is the case with delta distributions. The resulting velocity expression is called a regularized Stokeslet and the associated regularized rotlet was derived. These two types of elements were used to introduce the torque generated by the motors that rotate the flagella and the forces that provide elasticity to the flagella. The forces in the model presented here

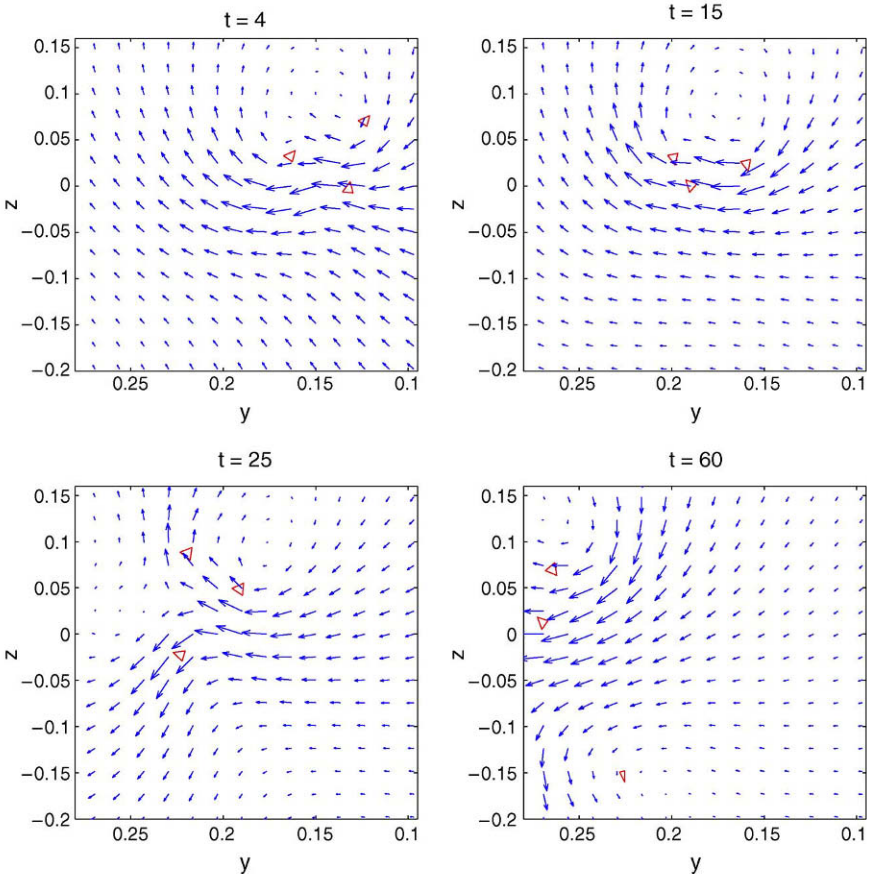

Fig. 20. The 20th cross section during the tumble.

are based on a network of springs of a given resting length and stiffness; however, other elasticity models can easily be used.

The tests performed for a single flagellum document the effect of different parameters on its motion. In general, the applied torque at a single location at the front of the flagellum introduces the rotation and the elastic forces maintain the structural integrity of the flagellum. The helical shape and the rotation necessarily generate forward swimming motion in a Stokes flow. The values for some of the parameters that lead to a faster swimming speed were estimated. In particular, the results show that the maximum swimming speed is achieved when the pitch of the helix has a given value regardless of the length of the flagellum. In addition, the linear dependence of the swimming and angular speeds on the torque was verified. The proportionality constants in these relations depend on numerical parameters such as the regularization parameters δ_s and δ_r. Since these represent the spreading distance of the forces and torques, they should be comparable

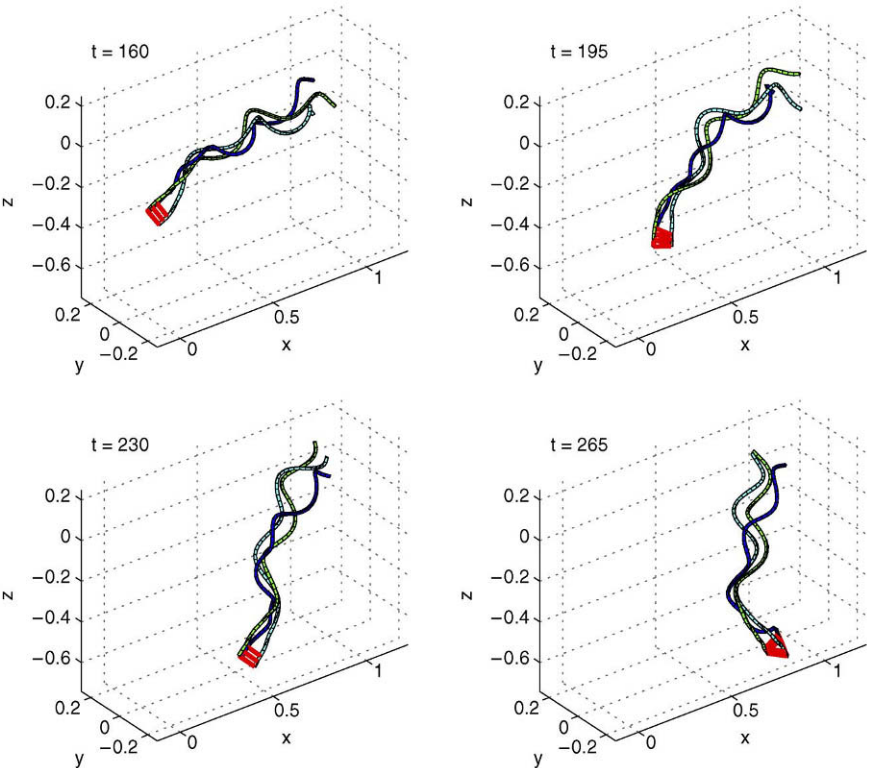

Fig. 21. Motion of the flagella during tumbling. This motion follows the bundling period of $t = 0$–0.0135 s shown in Fig. 17.

in size to the flagellar radius. More specific details of the dependence of errors on the numerical parameters can be found in Cortez et al. (in press).

The far-field velocity is not significantly affected by the regularization. Therefore, away from the front of the flagellum where the torques are located, the effect of the forces is more substantial than the effect of the torque since the rotlet expression decays faster than the Stokeslet expression as a function of distance. Of course, the forces depend implicitly on the torque since the entire system is coupled. The fluid flow surrounding the flagellum shows the rotation of the cross-sections and also shows circulation regions of alternating sign coincident with the helix wavelength (see Fig. 7).

The model was then applied to three interacting flagella. The front sections of the flagella were kept approximately at a fixed distance in order to simulate their connection to the bacterial body. In order to analyze the hydrodynamic interaction of the flagella without artificially revolving them around one another, a counter-torque was added to cancel the rotation of each flagellum around the others that the motors generate. The counter-torque can also be thought of as the effect of the counter-rotating bacterial body, which is currently not part of the model. One direction of future research is to include the

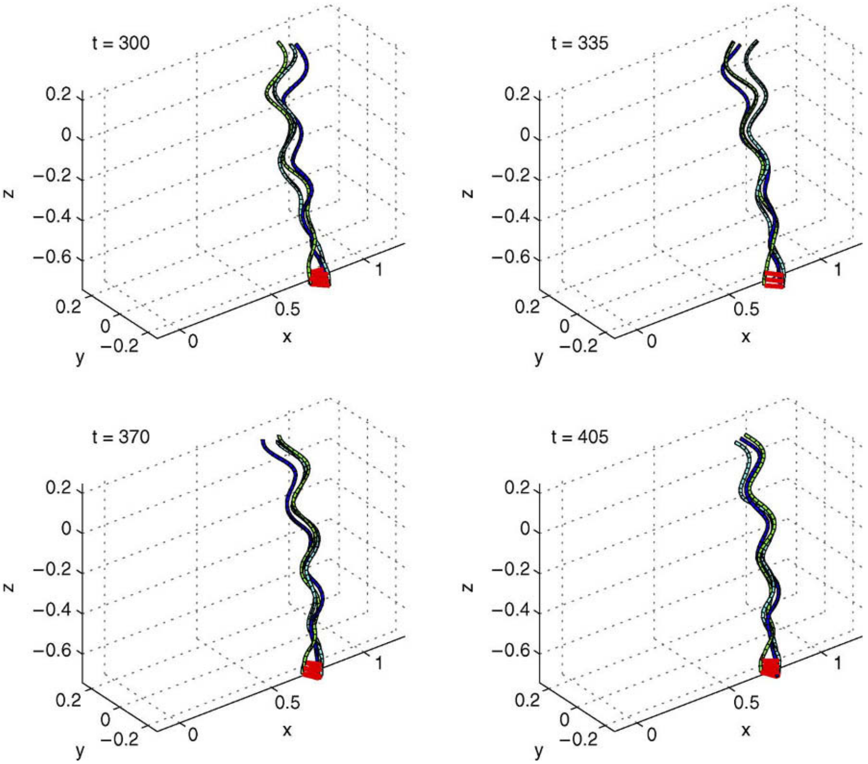

Fig. 22. Motion of the flagella during a second bundling period. This motion follows the tumbling period of $t = 0.0135$–0.0270 s shown in Fig. 21.

body and its appropriate counter-rotation. The main goal of the current work was to show the hydrodynamic interactions of flagella over short time scales.

When the three flagellar motors rotate counterclockwise, the hydrodynamic interaction of the flagella can lead to bundling. Our results show that the flow near the front of the flagella is mainly a combination of all the torques, which have comparable magnitude. Further away from the front, the flow on planes perpendicular to the axes of the flagella appears to become a single rotation whose center is outside the triangle defined by the three flagellar cross-sections (see Fig. 14). This flow causes the flagella to rotate in circles as a unit but also draws them closer together, resulting in bundling. In this case the structure maintains its orientation. These results clearly show that the fluid flow generated by the flagella draws them together and point to the importance of accounting for the fluid dynamics when modeling the bundling process.

When one or two of the motors turns in the opposite direction, the flow patterns change dramatically. The generated flow near the cross-sections has a counter-rotating character, which causes the flagella to separate and forces the front sections to change their orientation erratically consistent with tumbling. There is no significant net forward motion in this case and the tumbling occurs in a faster time scale than bundling. When the motors are returned to their counterclockwise motion, the flagella bundle again tightly.

In the future, we expect to improve the model for long-term motions of the bacteria, including their heads and flagella. We expect to incorporate information about the internal structure of the flagella into the spring model more accurately and use flagella with more realistic proportions (longer). To accomplish this, some aspects of the efficiency of the numerical method will also need to be addressed. Finally, a thorough comparison between the numerical method presented here and other methods, such as local resistive-force theory and slender-body theories, would be very instructive to assess any differences, limitations and strengths of each method.

Acknowledgements

This work was funded by NSF grant #DMS-0094179. The work was conducted in the Center for Computational Science at Tulane and Xavier Universities which is supported in part by DOE grant #DE-FG02-01ER63119.

Appendix A

A.1. Derivation of the regularized Stokeslet

The Stokes equations are

$$0 = -\nabla P + \Delta \mathbf{u} + \mathbf{f} \tag{A.1}$$

$$0 = \nabla \cdot \mathbf{u}. \tag{A.2}$$

We assume that the force is given by $\mathbf{f}(\mathbf{x}) = \mathbf{f}_0 \phi_\delta(\mathbf{x} - \mathbf{x}_0)$. For simplicity we assume $\mathbf{x}_0 = 0$ and we write $r = \|\mathbf{x}\|$.

We take the divergence of Eq. (A.1) and use Eq. (A.2) to eliminate the velocity and get an equation for the pressure

$$\Delta P = \nabla \cdot \mathbf{f} = \mathbf{f}_0 \cdot \nabla \phi_\delta$$

whose solution is

$$P(\mathbf{x}) = \mathbf{f}_0 \cdot \nabla G_\delta(\mathbf{x}), \qquad \text{where } \Delta G_\delta = \phi_\delta.$$

Substituting this expression for $p(\mathbf{x})$ into Eq. (A.1) results in the following equation for the fluid velocity

$$\Delta \mathbf{u} = (\mathbf{f}_0 \cdot \nabla)\nabla G_\delta - \mathbf{f}_0 \phi_\delta$$

whose solution is

$$\mathbf{u}(\mathbf{x}) = (\mathbf{f}_0 \cdot \nabla)\nabla B_\delta(\mathbf{x}) - \mathbf{f}_0 G_\delta(\mathbf{x}), \qquad \text{where } \Delta B_\delta = G_\delta.$$

For the particular cutoff function used throughout this article

$$\phi_\delta(\mathbf{x}) = \frac{15\delta^4}{8\pi(r^2 + \delta^2)^{7/2}}$$

we have that

$$P(\mathbf{x}) = (\mathbf{f}_0 \cdot \mathbf{x}) \frac{2r^2 + 5\delta^2}{8\pi (r^2 + \delta^2)^{5/2}} \tag{A.3}$$

and

$$\mathbf{u}(\mathbf{x}) = \mathbf{f}_0 \frac{r^2 + 2\delta^2}{8\pi (r^2 + \delta^2)^{3/2}} + \frac{(\mathbf{f}_0 \cdot \mathbf{x})\mathbf{x}}{8\pi (r^2 + \delta^2)^{3/2}}. \tag{A.4}$$

Eq. (A.4) is also displayed as Eq. (5).

A.2. Derivation of the regularized rotlet

We begin with the regularized Stokeslet found in the previous section, Eq. (A.3) and (A.4).

$$P_0 = \frac{(5\delta^2 + 2r^2)(\mathbf{f}_0 \cdot \mathbf{x})}{8\pi (r^2 + \delta^2)^{5/2}}, \qquad \mathbf{U}_0 = \frac{\mathbf{f}_0 (r^2 + 2\delta^2)}{8\pi (r^2 + \delta^2)^{3/2}} + \frac{(\mathbf{f}_0 \cdot \mathbf{x})\mathbf{x}}{8\pi (r^2 + \delta^2)^{3/2}}$$

where $\mathbf{f}_0$ is an arbitrary vector constant. Now, $(P_0, \mathbf{U}_0)$ satisfy $\nabla P_0 = \Delta \mathbf{U}_0 + \mathbf{f}_0 \phi_\delta$. Other solutions can be found by differentiation. For example, let $\mathbf{g}$ be an arbitrary constant vector, and define

$$P_1 = \mathbf{g} \cdot \nabla P_0 \qquad \textit{and} \qquad \mathbf{U}_1 = (\mathbf{g} \cdot \nabla)\mathbf{U}_0.$$

One can check that $(P_1, \mathbf{U}_1)$ are solutions of the Stokes equations with forcing term $(\mathbf{g} \cdot \nabla)\mathbf{f}_0 \phi_\delta$. If we expand $\mathbf{U}_1$ using Eq. (A.4), we obtain

$$\begin{aligned} \mathbf{U}_1 = {} & \frac{-(r^2 + 4\delta^2)}{8\pi (r^2 + \delta^2)^{5/2}} (\mathbf{g} \cdot \mathbf{x})\mathbf{f}_0 + \frac{1}{8\pi (r^2 + \delta^2)^{3/2}} (\mathbf{f}_0 \cdot \mathbf{x})\mathbf{g} \\ & + \frac{(\mathbf{g} \cdot \mathbf{f}_0)\mathbf{x}}{8\pi (r^2 + \delta^2)^{3/2}} - \frac{3(\mathbf{f}_0 \cdot \mathbf{x})(\mathbf{g} \cdot \mathbf{x})\mathbf{x}}{8\pi (r^2 + \delta^2)^{5/2}}. \end{aligned} \tag{A.5}$$

We look for the antisymmetric part of this expression with respect to $\mathbf{f}_0$ and $\mathbf{g}$. Notice that the third and fourth terms on the right side of Eq. (A.5) are symmetric with respect to $\mathbf{f}_0$ and $\mathbf{g}$ (switching $\mathbf{f}_0$ and $\mathbf{g}$ makes no difference). To determine the symmetry in terms one and two, we may write them as

$$\frac{(a+b)}{2}[(\mathbf{g} \cdot \mathbf{x})\mathbf{f}_0 + (\mathbf{f}_0 \cdot \mathbf{x})\mathbf{g}] + \frac{(a-b)}{2}[(\mathbf{g} \cdot \mathbf{x})\mathbf{f}_0 - (\mathbf{f}_0 \cdot \mathbf{x})\mathbf{g}]$$

where

$$a = \frac{-(r^2 + 4\delta^2)}{8\pi (r^2 + \delta^2)^{5/2}} \qquad \text{and} \qquad b = \frac{1}{8\pi (r^2 + \delta^2)^{3/2}}.$$

Therefore, the antisymmetric part of Eq. (A.5) is

$$\begin{aligned} \mathbf{U}_{\delta,r}(\mathbf{x}) &= \frac{(a-b)}{2}[(\mathbf{g} \cdot \mathbf{x})\mathbf{f}_0 - (\mathbf{f}_0 \cdot \mathbf{x})\mathbf{g}] \\ &= \frac{-(2r^2 + 5\delta^2)}{8\pi (r^2 + \delta^2)^{5/2}}[(\mathbf{g} \cdot \mathbf{x})\mathbf{f}_0 - (\mathbf{f}_0 \cdot \mathbf{x})\mathbf{g}]. \end{aligned}$$

Defining $\mathbf{L} = \mathbf{f}_0 \times \mathbf{g}$, our equation for $\mathbf{U}_{\delta,r}$ becomes

$$\mathbf{U}_{\delta,r}(\mathbf{x}) = \frac{(2r^2 + 5\delta^2)}{16\pi(r^2 + \delta^2)^{5/2}}(\mathbf{L} \times \mathbf{x})$$

which is the equation given in Eq. (6). $\mathbf{U}_{\delta,r}$ represents the flow due to a regularized rotlet of strength $\mathbf{L}$. We mention that as δ approaches zero, we recover the singular form of the rotlet, Eq. (3). However, the regularized rotlet is a bounded function that can be evaluated everywhere.

References

Berg, H.C., 2003. The rotary motor of bacterial flagella. Annu. Rev. Biochem. 72, 19–54.

Berry, R.M., 2001. Bacterial flagella: Flagellar motor. In: Nature Encyclopedia of Life Sciences. Nature Publishing Group, http://www.els.net.

Cortez, R., 2001. The method of regularized Stokeslets. SIAM J. Sci. Comput. 23, 1204–1225.

Cortez, R., Fauci, L., Medovikov, A., 2004. The method of regularized Stokeslets in three dimensions: analysis, validation, and application to helical swimming. Phys. Fluids (in press).

Dillon, R., Fauci, L., 2000. An integrative model of internal axoneme mechanics and external fluid dynamics in ciliary beating. J. Theor. Biol. 207, 415–430.

Goto, T., Inaoka, R., Takano, Y., 1999. A boundary element analysis of swimming bacteria with several flagella. In: Proceedings of the Bioengineering Conference. ASME, Big Sky, Montana, June 16–20, 1999.

Goto, T., Masuda, S., Terada, K., Takano, Y., 2001. Comparison between observation and boundary element analysis of bacterium swimming motion. JSME Int. J. Ser. C 44, 958–963.

Gray, J., 1968. Animal Locomotion. Weidenfeld&Nicolson, London.

Higdon, J.J.L., 1979a. A hydrodynamic analysis of flagellar propulsion. J. Fluid Mech. 90, 685–711.

Higdon, J.J.L., 1979b. The hydrodynamics of flagellar propulsion: helical waves. J. Fluid Mech. 94, 331–351.

Jones, C.J., Aizawa, S.I., 1991. The bacterial flagellum and flagellar motor: structure, assembly and function. J. Mol. Biol. 32, 109–172.

Kamiya, R., Asakura, S., 1976. Helical transformations of salmonella flagella in vitro. J. Mol. Biol. 106, 167–186.

Kim, M.J., Bird, J.C., Van Parys, A.J., Breuer, K.S., Powers, T.R., 2003. A macroscopic scale model of bacterial flagellar bundling. Proc. Natl. Acad. Sci. USA 100, 15481.

Lighthill, M.J., 1976. Flagellar hydrodynamics. SIAM Rev. 18, 161–230.

Lighthill, M.J., 1996. Helical distributions of Stokeslets. J. Eng. Math. 30, 35–78.

Lim, S., Peskin, C.S., 2004. Simulations of the whirling instability by the immersed boundary method. SIAM J. Sci. Comput. 25, 2066–2083.

McClaine, J.W., Ford, R.M., 2002. Reversal of flagellar rotation is important in initial attachment of *Escherichia coli* to glass in a dynamic system with high- and low-ionic-strength buffers. Appl. Environ. Microbiol. 68, 1280–1289.

Peskin, C.S., 2002. The immersed boundary method. Acta Numeri. 11, 479–517.

Powers, T.R., 2002. Role of body rotation in bacterial flagellar motion. Phys. Rev. E 65, 040903(R).

Purcell, E.M., 1997. The efficiency of propulsion by a rotating flagellum. Proc. Natl. Acad. Sci. USA 94, 24–29.

Ramia, M., Tullock, D.L., Phan-Thien, N., 1993. The role of hydrodynamic interaction in the locomotion of microorganisms. Biophys. J. 65, 755–778.

Turner, L., Ryu, W.S., Berg, H.C., 2000. Real-time imaging of fluorescent flagellar filaments. J. Bacteriol. 182, 2793–2801.